

Oxygen Deficient α -MoO₃ with Promoted Adsorption and State-Quenching of H₂O for Gas Sensor: A DFT Study

Changmeng Huan^{1,2}, Pu Wang^{1,2}, Binghan He^{1,2}, Yongqing Cai^{3*}, Qingqing Ke^{1,2*}

¹School of Microelectronics Science and Technology, Sun Yat-sen university, Zhuhai 519082, China

²Guangdong Provincial Key Laboratory of Optoelectronic Information Processing Chips and Systems, Sun Yat-sen University, Zhuhai 519082, China

³Joint Key Laboratory of the Ministry of Education, Institute of Applied Physics and Materials Engineering, University of Macau, Taipa, Macau, China

* Corresponding authors

E-mail: yongqingcai@um.edu.mo; keqingq@mail.sysu.edu.cn

Abstract:

Semiconducting oxides with reducible cations are ideal platforms for various functional applications in nanoelectronics and catalysts. Here we report an ultrathin monolayer α -MoO₃ where tunable electronic properties and different gas adsorbing behaviors upon introducing the oxygen vacancies (V_O). The unique property of α -MoO₃ is that it contains three different types of oxygen atoms occupying three Wyckoff sites that are absent in other low-dimensional oxides and provides rich electronic hybridized states. The presence of V_O triggers intermediate state in the gap at ~ 0.59 eV below the conduction band minimum and reduces the work function dramatically, together with new excitations at near infrared. The realigned Fermi level associated with the dangling

state of V_O reduces the neighboring Mo atoms and affects the gas adsorption thereafter. The binding energy of H_2O molecules above V_O is 2.5 times up to -0.75 eV compared with that of perfect lattice site and trends of transfer of electrons also reverse. The latter is related with the shallow localized state in the band gap due to H_2O adsorbed above perfect MoO_3 which becomes quenched upon adsorbing at the V_O site. Those rich in-gap defective states in oxygen deficient MoO_3 , broadening the light absorption and promoting the uptake of water, are conducive to the application of α - MoO_3 for optoelectronics, photothermal therapy, and sensor of moisture.

Keywords: Monolayer α - MoO_3 , Oxygen vacancy, H_2O adsorption, Gas sensor, Optoelectronic

1. Introduction

Two-dimensional (2D) transition metal oxides (TMOs) have received considerable attention owing to their distinctive electronic properties as well as high specific surface area and rich active surface sites¹⁻⁶. Orthorhombic phase α - MoO_3 , a stable layered TMO, has been widely used as anode material for ion batteries (e.g., H^+ , Li^+ , Zn^{2+}) and supercapacitors due to its multiple valence states and unique layered structure⁷⁻⁹. Recently, anisotropic phonon polaritons and photonic magic angles were demonstrated in twisted α - MoO_3 , offering unprecedented opportunities for controlling light at the nanoscale and making the ultrathin α - MoO_3 an interesting subject in materials research¹⁰⁻¹³.

Significantly, electronic and optical properties of α -MoO₃ are highly tunable with oxygen vacancies (V_O). Associated with the enhanced electrical conductivity and additional active sites induced by V_O, MoO_{3-x} electrodes exhibit superior rate performance and excellent cycling stability¹⁴⁻¹⁶. Furthermore, the work function of α -MoO₃ is tunable with the defective levels induced by V_O, which has been utilized to design the MoS₂/ α -MoO_{3-x} heterojunction as phototransistors with a high detectivity of $9.8 \times 10^{16} \text{ cm Hz}^{1/2} \text{ W}^{-1}$ ¹⁷. Meanwhile, the defective levels can achieve near infrared (NIR) absorption and localized surface plasmon resonance (LSPR) effect, making α -MoO_{3-x} promising as biodegradable nanoagents for photothermal cancer therapy^{18, 19}.

On the other hand, α -MoO₃ has been demonstrated to be a promising material for gas sensing because of its high sensitivity, fast response and thermodynamic stability²⁰. Xu et al. have studied the adsorption behaviors of many gases (such as H₂, H₂S, NH₃, CO) molecules on the surface of MoO₃, providing a conceptual foundation for MoO₃-based gas sensor^{21, 22}. In addition, adsorbates from ambient conditions may cause degradation and affect the remarkable properties of the two-dimensional material, especially in the presence of vacancies²³⁻²⁶. Unfortunately, the effects of the V_O and its associated coupling with H₂O molecules in α -MoO₃ have been scarcely reported, and understanding the interplay of the structural defect and adsorbates is prerequisite for its massive applications.

In this work, we systematically studied the adsorption behavior of H₂O molecules on the surface and oxygen vacancies of monolayer α -MoO₃ through density functional theory (DFT) calculations, as well as the electronic properties, interfacial charge

transfer, work function, and optical properties. Our results indicate that the adsorption of H₂O molecules on the surface of α -MoO₃ will introduce an intermediate state close to the edge of valence band and allowing the thermally activated conduction, which is necessary for monitoring relative humidity in moisture-sensitive environment. For oxygen deficient α -MoO₃, the depletion of O atoms makes the dangling Mo atoms reduced and promotes the adsorption of H₂O. While the H₂O donates electrons to MoO₃ for adsorbing above perfect lattice, it accepts electrons when adsorbing above V_O site. This strong interaction between V_O-H₂O complex makes oxygen deficient MoO_{3-x} a promising moisture sensor. Moreover, the rich in-gap defective states in oxygen deficient MoO₃ can modulate the work function and carrier density, broaden the light absorption, and promote the uptake of water, which highlights the prospect of α -MoO₃ as tunable optoelectronics, photothermal and sensing materials.

2. Computational method and details

The first-principles calculations based on the projected augmented wave (PAW) method as implemented in Vienna Ab Initio Simulation Package (VASP) were employed^{27, 28}. The Perdew-Burke-Ernzerhof (PBE) functional of the generalized gradient approximation (GGA) was used to treat the exchange and correlation²⁹. Since the pure DFT is less accurate to describe van der Waals (vdW) interactions, the geometric structures were fully relaxed through PBE functional with vdW-D3 correction^{30, 31}. The plane-wave cutoff energy of 400 eV and a Monkhorst-Pack k-points sampling of $3 \times 3 \times 1$ for the $4 \times 4 \times 1$ monolayer supercell were adopted. A vacuum layer of 15 Å in z

direction was inserted to avoid mirror interactions. The structural optimizations were considered to be converged when the system energies and Hellman-Feynman force on each atom were less than 1×10^{-6} eV and 0.01 eV/Å, respectively. Since the PBE method seriously underestimates the band gap, we utilized the standard Heyd-Scuseria-Ernzerhof (HSE06) hybrid functional to calculate the electronic structure and optical properties³². The effective band structures were calculated by the corresponding module in VASPKIT³³.

In Van de Walle method, the formation energy (E_f) of oxygen vacancies is calculated through³⁴

$$E_f = E_d - E_p + n_O \mu_O \quad (1)$$

where E_d and E_p represent the total energies of the defective and perfect α -MoO₃, respectively, n_O indicates the number of V_O, and μ_O is the chemical potential of O atom. The range of μ_O in MoO₃ can be expressed as³⁵

$$\mu_O(\text{Mo-rich}) < \mu_O^{\text{MoO}_3} < \mu_O(\text{O-rich}) \quad (2)$$

where $\mu_O(\text{O-rich})$ represent the oxygen chemical potentials equals to μ_O^O of O₂ molecular (per oxygen atom). $\mu_O(\text{Mo-rich}) = \mu_O^O + \Delta E_f^{\text{MoO}_3}$ corresponds to the Mo-rich conditions and the $\Delta E_f^{\text{MoO}_3}$ is the formation energy of MoO₃ from metal Mo and O₂ gas. If the charged defects are considered, the formation energy (E_f) formula should be extended as³⁶

$$E_f = E_d - E_p + n_O \mu_O + q (E_F + E_V + \Delta V) \quad (1)$$

where E_F is the Fermi level referenced to the energy of the VBM (E_V) in perfect MoO₃, ranging from 0 to the value of the band gap. A correction term ΔV was added to align the reference electrostatic potential in defective MoO₃ with that in perfect MoO₃.

The adsorption energies (E_{ads}) of H₂O molecule on α -MoO₃ systems are calculated as³⁷

$$E_{\text{ads}} = E_{\text{i+w}} - E_{\text{i}} - E_{\text{w}} \quad (3)$$

where $E_{\text{i+w}}$, E_{i} , and E_{w} represent the energies of H₂O adsorbed α -MoO₃, the pristine α -MoO₃, and the isolated H₂O molecule, respectively.

3. Results and Discussion

Pristine perfect α -MoO₃ monolayer:

The crystal structure of bulk α -MoO₃ (Fig. 1a) belongs to the orthorhombic $Pbnm$ space group, which consists of alternating layers with corner-sharing and distorted MoO₆ octahedrons. There are merely weak vdW interactions between adjacent monolayers, therefore the monolayer α -MoO₃ (Fig. 1b) can be acquired through mechanical cleavage along the (010) plane. As marked in Fig. 1c and d, the distorted MoO₆ octahedron has three distinct oxygen sites: terminal oxygen (O_t), asymmetric oxygen (O_a), and symmetric oxygen (O_s). In the optimized bulk α -MoO₃, the O_t atoms is exclusively coordinated with one Mo atom with a bond length of 1.70 Å. The O_a atoms are 2-fold coordinated forming a relatively long (2.21 Å) and short (1.77 Å) bonds with Mo atoms in the same layer. The O_s atoms are tri-coordinated forming two equal bonds (1.95 Å) with Mo atoms in the same layer and a much longer bond (2.38 Å) with one Mo atom in the other sublayer. As shown in Table 1, the calculated lattice parameters and M-O bond length for bulk MoO₃ in this work are in line with those of previous theoretical work and experiment^{21, 38}. In the monolayer case, the bond (2.47 Å) between

O_s and Mo atoms in the other sublayer is slightly longer than that in bulk of 2.38 Å.

This reflects the relaxation of the lattice in monolayer due to the disappearing of the interlayer interactions as presence in bulk α - MoO_3 .

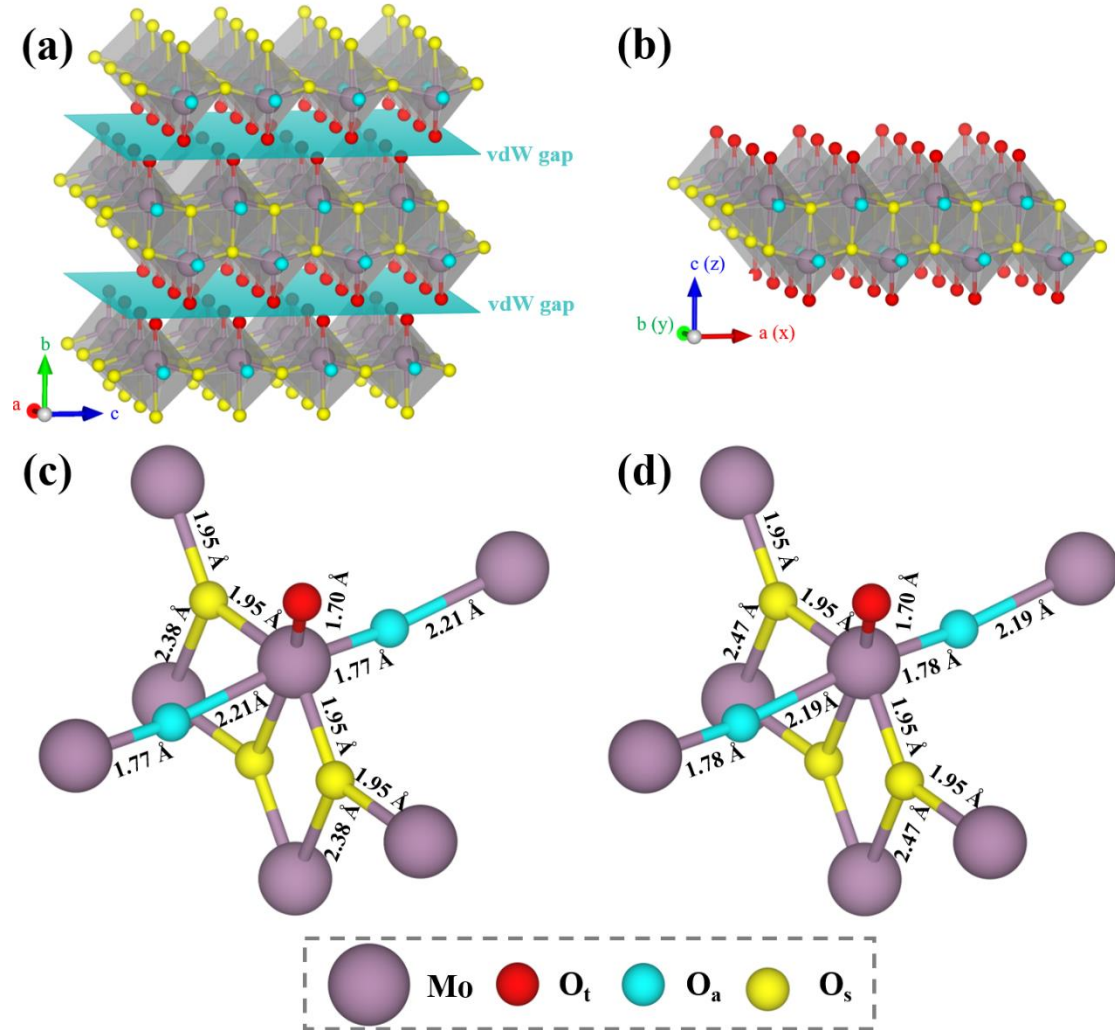


Fig. 1 Structure of the optimized bulk α - MoO_3 supercell (a) along the [010] orientation and monolayer α - MoO_3 supercell (b). The distorted MoO_6 octahedrons with nearest neighbor Mo atoms in bulk (c) and monolayer (d) highlighting the oxygen sites and bond length.

Table 1. Calculated lattice parameters and M-O bond length for bulk and monolayer α -

MoO₃ compared to previous theoretical work and experiment.

Structure	Bulk	Monolayer Supercell	Bulk ²¹ (Previous work)	Bulk ³⁸ (Experiment)
a (Å)	3.96	/	3.96	3.96
b (Å)	13.86	/	13.86	13.86
c (Å)	3.70	/	3.70	3.70
d _{Mo-O_t} (Å)	1.70	1.70	1.68	1.67
d _{Mo-O_a 1} (Å)	1.77	1.78	1.75	1.73
d _{Mo-O_a 2} (Å)	2.21	2.19	2.24	2.25
d _{Mo-O_s 1} (Å)	1.95 (2×)	1.95 (2×)	1.95 (2×)	1.95 (2×)
d _{Mo-O_s 2} (Å)	2.38	2.47	2.38	2.33

Energetics of oxygen vacancies in monolayer α -MoO₃:

Transition metal oxides have a tendency to form oxygen vacancies which have profound influence on their physical and chemical properties^{39, 40}. In the monolayer α -MoO₃ supercell, three types of oxygen vacancies can therefore be considered and calculated through removing the oxygen atoms lying on the terminal, asymmetric and symmetric sites. The formation energies of three types of V_O and geometry structure of oxygen deficient MoO₃ systems were calculated and presented in Table 2 and Fig. 2, respectively. We found that both V_{O_t}-MoO₃ and V_{O_a}-MoO₃, showing similar structure after relaxation and same energy, are around 2.15 eV lowered in total energy than that of the V_{O_s}-MoO₃. This indicates that V_{O_t} and V_{O_a} are more energetically favored compared with V_{O_s}-MoO₃. As shown in Fig. 2(a-c), the formation of V_O leads to a strong geometrical rearrangement around V_O. For V_{O_t}-MoO₃, the nearest O_a atom moves towards the V_{O_t} while the dangling Mo atom downshift, causing the bond length

of Mo-O_a to decrease from 2.19 and 1.78 Å to 1.80 and 1.70 Å, respectively. Meanwhile, bond length of the dangling Mo with the O_s in the other sublayer reduces from 2.47 to 2.18 Å. More importantly, our results demonstrate that V_{Ot}- and V_{Oa}-MoO₃ show similar geometry structure (the remaining O atom stays at an intermediate position between initial O_t and O_a sites) and the same formation energies after relaxation. The negative E_f of V_O in Mo-rich (O-poor) conditions indicates that the formation of V_O in a reducing atmosphere or ultra-high vacuum is energetically favored, which is consistent with the similar trends of V_O in wide bandgap semiconductors⁴¹. Our work suggests that the production of the V_O spans a broad range of the oxygen chemical potential which allows flexible modulation and control of its content and distribution such defects via external pressures and temperatures.

Table 2. The relative energies (ΔE_0) of different MoO₃ systems and the formation energies of different oxygen vacancies in PBE method, where the total energy of V_{Os}-MoO₃ is set to zero for comparison

	V _{Ot} -MoO ₃	V _{Oa} -MoO ₃	V _{Os} -MoO ₃
ΔE_0 (eV)	-2.15	-2.15	0
E_f (Mo-rich) (eV)	-5.72	-5.72	-3.57
E_f (O-rich) (eV)	2.08	2.08	4.23

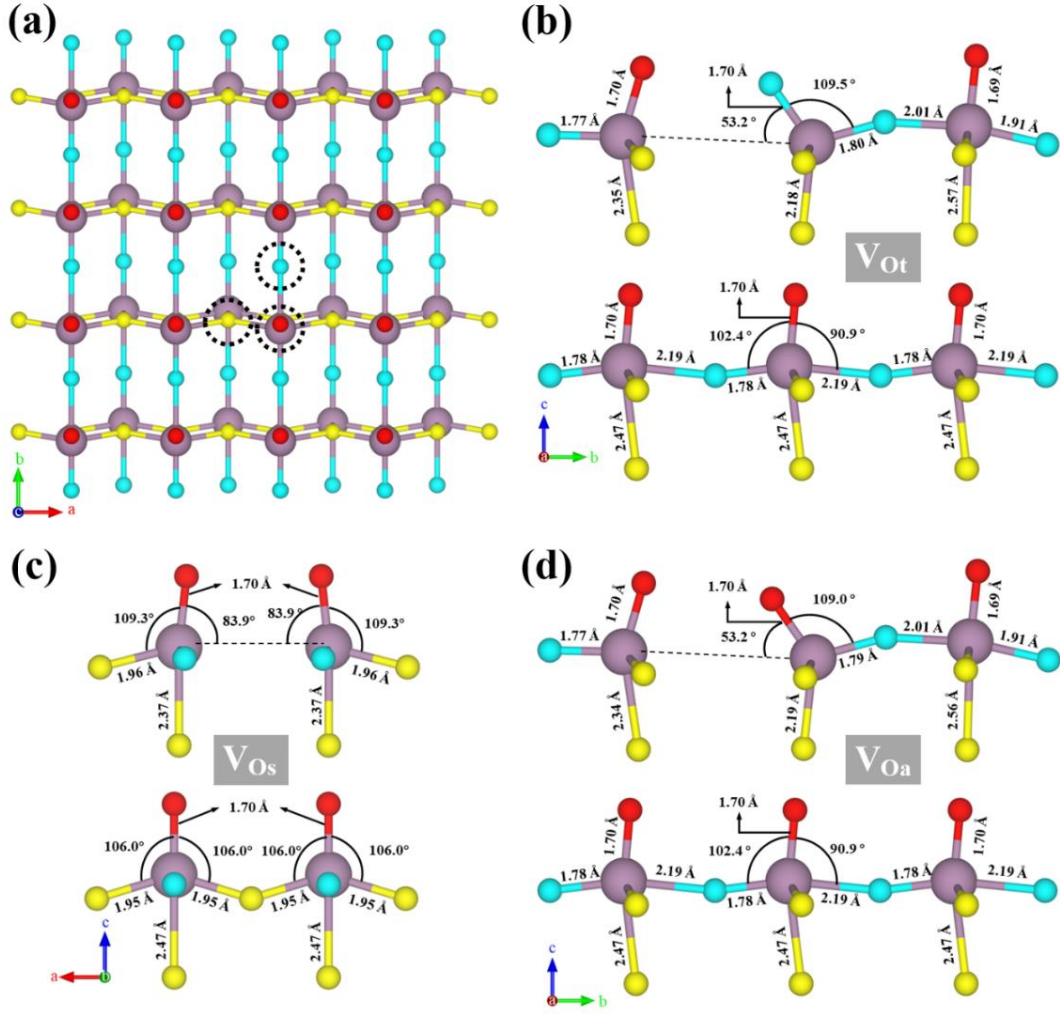


Fig. 2 (a) Top view of the monolayer α - MoO_3 supercell marked with three types of oxygen sites. The structural features of the optimized and pristine $\text{V}_{\text{Ot}}\text{-MoO}_3$ (b), $\text{V}_{\text{Os}}\text{-MoO}_3$ (c), and $\text{V}_{\text{Oa}}\text{-MoO}_3$ (d) system.

For analysis and comparison, charged oxygen vacancies are also considered. The results in Fig. S1 and Table. S1 show that V_{O}^0 are more thermodynamically favored than V_{O}^{1+} and V_{O}^{2+} in oxygen deficient α - MoO_3 (n-type semiconductor). Furthermore, the adsorption behavior, electronic and optical properties of $\text{V}_{\text{Ot}}\text{-MoO}_3$ and $\text{V}_{\text{Oa}}\text{-MoO}_3$ (Fig. S2) are the same. Therefore, only charge-free $\text{V}_{\text{Ot}}\text{-MoO}_3$ will be considered in the following discussions.

Adsorption of H₂O molecule:

The adsorbates from ambient conditions may influence the electronic and optical properties of 2D materials, herein, the adsorption behavior of H₂O on the surface of α -MoO₃ systems is considered. H₂O molecules are polar molecules, with negative charge (σ^-) on the O atom side and positive charge (σ^+) on H atom side. According to the principle of mutual attraction between (σ^+) and (σ^-), five possible adsorption sites of H₂O above perfect MoO₃ are considered in Fig. S3. In site 1, one arm of H-O-H vertically pointing to a O_t of MoO₃. In site 2 and 3, the H-O-H are located above the center of the two O_t atoms along the O_a and O_s arrangement direction, respectively. In site 4 and 5, the H-O-H atoms are located diagonally above the center of the rectangle formed by four O_t atoms with O-H bonds pointing up and down, respectively. Based on the lowest-energy configuration, the total energies and adsorption energies of final structure are summarized in Table S2. The most stable configuration (E_{ads} of -0.30 eV) is at site 4, where the oxygen of the water slightly deviates above the center of the rectangle formed by four O_t atoms with two O-H bonds pointing up. The uptake of more water molecules on the surface were also calculated. To compare the trend, we examined higher coverages with the adsorption of 1 to 4 H₂O molecules on the surface of α -MoO₃, and the results are shown in Table 3. The adsorption energies increase almost linearly with the increase in the number of H₂O, and the average adsorption energy per molecule H₂O remains basically unchanged. As shown in Fig. 3 (a), the structure and parameters of 4-H₂O adsorbed α -MoO₃ systems are basically consistent

with 1-H₂O adsorbed α -MoO₃ (Fig. S3 site 4), which means a strong adsorption capacity on the surface of monolayer α -MoO₃. These coplanar and equally separated of adsorption of adsorbed H₂O would favor the proton hopping in hydrated MoO₃. The shallow defective states arisen from H₂O in the band gap of MoO₃ also alter the behaviors of charge dynamics as we shown below.

Table 3. The adsorption energies (E_{ads}) of perfect and defective α -MoO₃ systems, where $E_{\text{ads-A}}$ represents the average adsorption energies per molecule H₂O.

	1-H ₂ O	2-H ₂ O	3-H ₂ O	4-H ₂ O	V _O -H ₂ O
E_{ads} (eV)	-0.30	-0.60	-0.87	-1.15	-0.75
$E_{\text{ads-A}}$ (eV)	-0.30	-0.30	-0.29	-0.29	-0.75

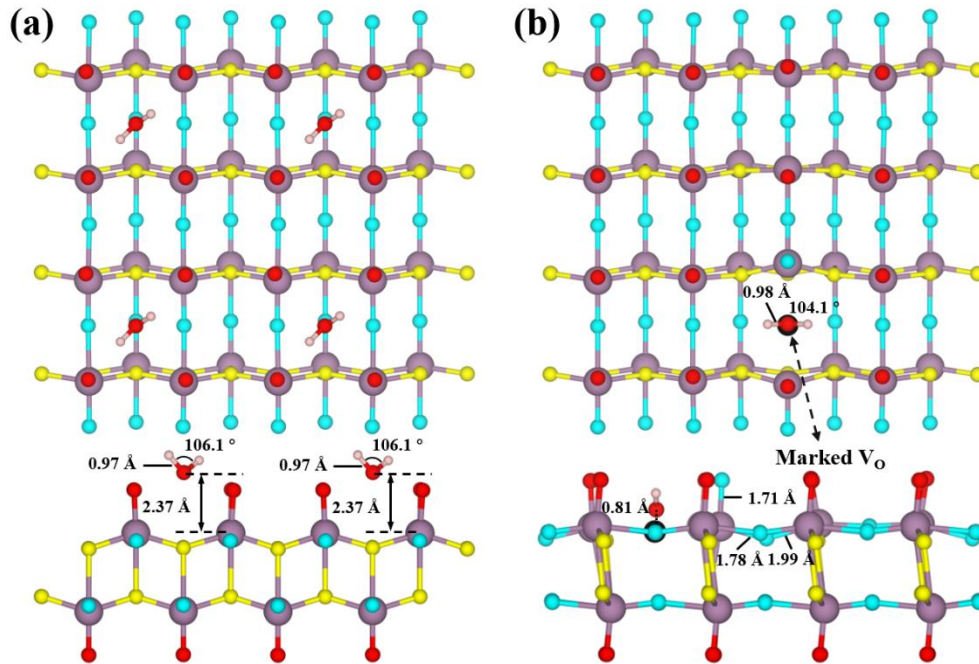


Fig. 3 Top and side views of the optimized structures of 4-H₂O molecules on the surface of perfect-MoO₃ (a) and H₂O molecule on the surface of V_Ot-MoO₃ (b). The red and pink balls represent O and H atoms, respectively.

To study the adsorption behavior of H₂O molecule at V_O, we obtained the optimized structure from an initial structure in which H₂O molecule is located at the marked V_O site (Fig. 3b). As shown in Table 3, the presence of V_O on the surface significantly promotes the adsorption of H₂O molecules. The E_{ads} for V_O-MoO₃ (-0.75 eV) is 2.5 times the values for perfect-MoO₃ with lowest configurations at site 4 (-0.30 eV). In addition, in Fig. 3 (b), the adsorption of H₂O also restores the bond lengths of certain Mo-O bonds in V_O-MoO₃ toward the values for perfect-MoO₃. This suggests that the adsorbed H₂O could partially passivate the V_O.

The relatively large dipole moment of H₂O is liable to induce a charge redistribution in the adsorbed α -MoO₃ surface. To analyze the electronic interaction between the H₂O molecule with the MoO₃, we conducted a calculation on the differential charge density (DCD) $\Delta\rho(r)$ defined as the difference between the total charge density of H₂O adsorbed MoO₃ system minus the sum of the charge density of the isolated H₂O molecule and MoO₃ system (perfect-MoO₃ or V_O-MoO₃). To obtain the exact amount of transferred charge, the plane-averaged DCD $\Delta\rho(z)$ along the normal direction (z) direction of MoO₃ system is calculated by integrating $\Delta\rho(r)$ within the basal plane at the z point. The amount of transferred charge at z point is given by $\Delta Q(z) = \int_{-\infty}^z \Delta\rho(z') dz'$ ^{42, 43}. Based on the $\Delta Q(z)$ curves, the total amount of charge donated by the molecule is read at the interface between the H₂O and the MoO₃ system, where $\Delta\rho(z)$ shows a zero value.

The isosurfaces of $\Delta\rho(r)$ for the H_2O molecule adsorbed on perfect MoO_3 and V_O - MoO_3 are plotted in Fig. 4, respectively. Fig. 4a shows that there is a depletion of electrons in H_2O molecule and an accumulation of electrons in the nearest O atoms of perfect MoO_3 surface, and the H_2O molecule donates electrons to α - MoO_3 with 0.02 e per molecule. For the MoO_3 surface decorated with four H_2O molecules, the electrons transfer from H_2O molecules to α - MoO_3 is up to 0.09 e with about 0.02 e per molecule, which is consistent with the linear increase of adsorption energy in Table 3. This trend is same to the slightly positively charge of H_2O above phosphorene but different from those adsorptions above graphene and antimonene⁴⁴. In contrast, for H_2O adsorbing above V_O (V_O - MoO_3 - H_2O), there is an accumulation of electrons in H_2O molecule and a depletion of electrons in the nearest Mo atoms of V_O - MoO_3 , and the H_2O molecule accepts electrons from V_O - MoO_3 with around 0.06 e per molecule (Fig. 4b), which results from the occupied Mo $4d_{xy}$ gap state introduced by V_O (see next section). The charge transfer from this localized state induced by V_O to the H_2O molecule is more likely to occur⁴⁵. Therefore, the presence of V_O could alter the energetics and charged state of adsorbed H_2O . The presence of H_2O and V_O may significantly affect the properties such as carrier density and mobility which is appealing for sensor of moisture.

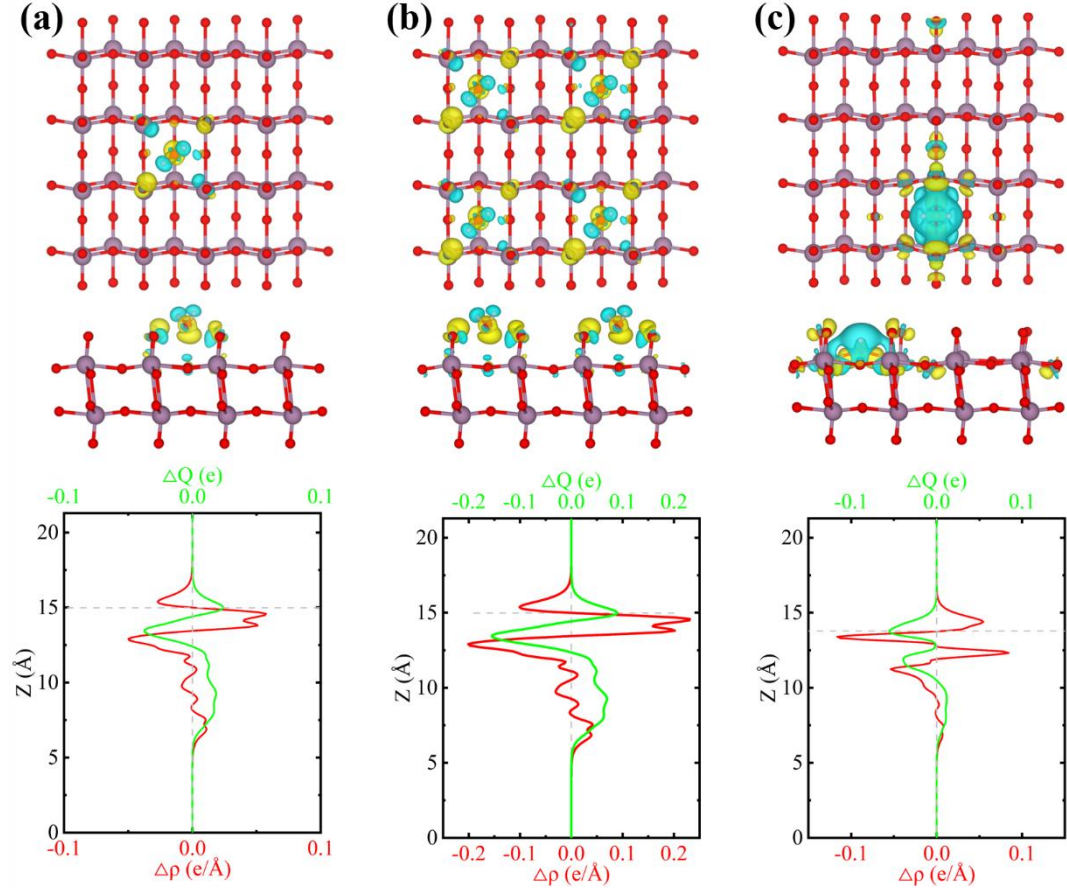


Fig. 4 Charge redistribution for $\text{MoO}_3\text{-H}_2\text{O}$ (a), $\text{MoO}_3\text{-4H}_2\text{O}$ (b), and $\text{V}_\text{O}\text{-MoO}_3\text{-H}_2\text{O}$ (b). Top and middle panels: Top and front views of the DCD isosurfaces, where the cyan (yellow) region represents depletion (accumulation) of electrons. Bottom panel: Plane-averaged DCD $\Delta\rho(z)$ (red line) and the amount of transferred charge $\Delta Q(z)$ (green line) between the H_2O molecule and MoO_3 .

V_O and H_2O induced changes of electronic states:

The band structures of perfect- MoO_3 , perfect- MoO_3 adsorbed H_2O ($\text{MoO}_3\text{-H}_2\text{O}$), $\text{V}_\text{O}\text{-MoO}_3$, and $\text{V}_\text{O}\text{-MoO}_3\text{-H}_2\text{O}$ were calculated using HSE06 method. The CBM and valence band maximum (VBM) of Perfect- MoO_3 are 9.60 eV and 6.67 eV below the vacuum (Fig. 5a), respectively, together with an indirect bandgap of 2.92 eV, which are

consistent with the previous results obtained by ultraviolet photoemission spectroscopy (UPS) and inverse photoemission spectroscopy (IPES) in bulk⁴⁶⁻⁴⁸. Interestingly, the adsorption of H₂O molecule introduces an intermediate gap state at ~0.30 eV above the VBM (Fig. 5b) and maintain a band gap of 2.92 eV consistent with perfect-MoO₃. The relatively shallow state would trap the holes and alter the carrier dynamics in MoO₃. The H₂O molecule induced intermediate gap state in MoO₃ has not been found in other 2D systems like phosphorene and antimonene⁴⁴, where there is no water induced states in the band gap.

For oxygen deficient MoO₃, the formation of V_{Ot} introduces a gap state at ~0.59 eV below the CBM and reduces the bandgap from 2.92 to 2.81 eV, which is consistent with experimental result⁴⁹. This is due to the fact that the electrons transfer from the V_O to the 4d states of Mo sufficiently reduces the crystal field⁵⁰. Absorbingly, the intermediate state associated with H₂O above perfect MoO₃ disappears for H₂O adsorbed above V_O-MoO₃, leaving an intermediate state at ~0.57 eV below the CBM in Fig. 5d. These intermediate gap states in V_O-MoO₃ and V_O-MoO₃-H₂O could be responsible for the broadened window of light-absorption⁵¹.

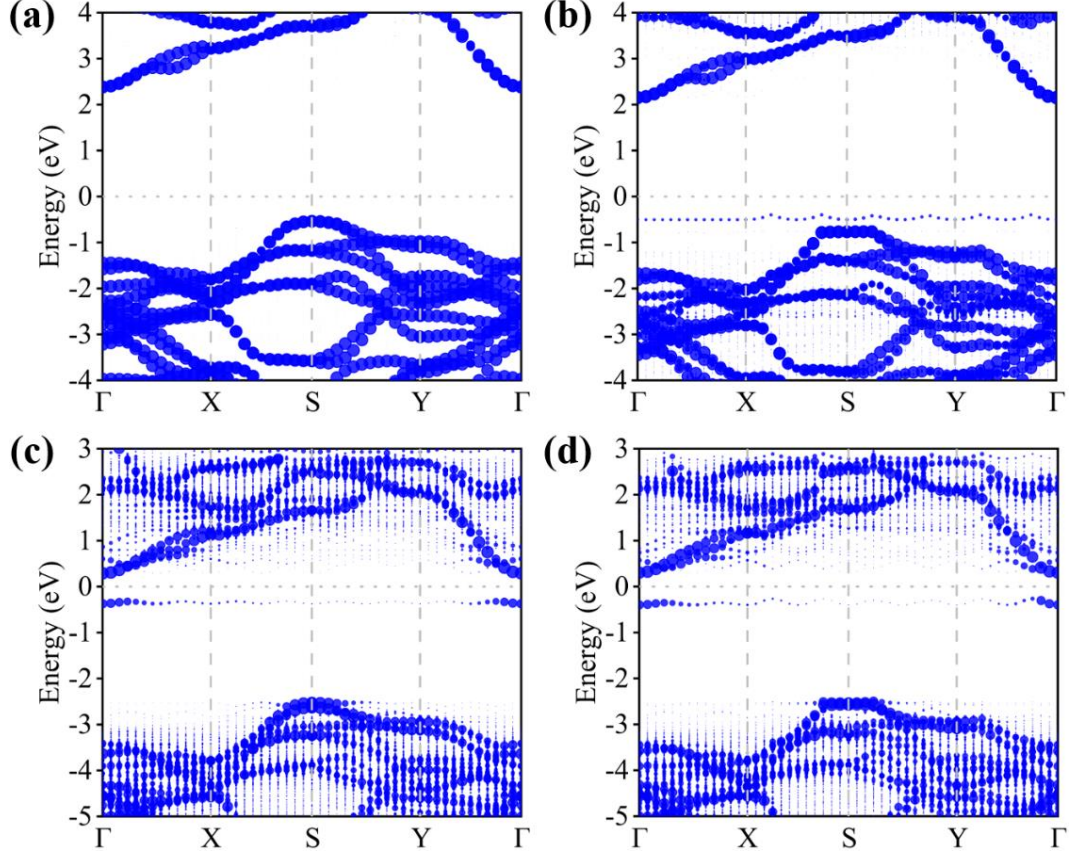


Fig. 5 Effective band structures for different α -MoO₃ systems acquired from HSE06 method, (a) perfect-MoO₃, (b) MoO₃-H₂O, (c) V₀-MoO₃, and (d) V₀-MoO₃-H₂O. The Fermi energy is set to zero and marked with a horizontal dashed line.

The projected density of states (PDOS) of different α -MoO₃ systems obtained from HSE06 method are shown in Fig. 6. In all systems, the top of the valence band (VB) is mainly composed of O 2p orbitals, while the bottom of the conduction band (CB) is characterized by Mo 4d states, which are in good agreement with previous study⁵⁰. Comparing Fig. 6a and b, it can be found that an intermediate state appears near the VBM after adsorbing H₂O which is mainly attributed to the 2p_x and 2p_y orbitals of O in H₂O, which increases the contribution to the VBM. Furthermore, as the number of adsorbed H₂O molecules increases, the water-induced shallow state becomes

stronger and extends to the edge of valence band (Fig. 6c), facilitating a promoted conductivity of the systems, which is necessary for H₂O sensing. The same phenomenon occurs in NO₂ adsorbed silicon oxycarbide⁵².

In Fig. 6d and e, there are occupied gap states near the CBM in both the V_O-MoO₃ and V_O-MoO₃-H₂O, which serve as donor levels in the bandgap, giving rise to a significant up-shift in the Fermi level and making the systems n-type. The formation of V_{Ot} donates 2e to the Mo-4d states, which reduces the crystal field and results in the formation of an extended 4d_{xy} gap state (inset in Fig. 6)²⁰. Consistent with the effective band structure (Fig. 5), the H₂O related shallow state quenches and disappears upon H₂O adsorbing above V_O. Interestingly, compared with the naked V_O-MoO₃, the addition of H₂O effectively promotes the DOS at the band edges of CB and VB. This in turn will increase the number of charged carriers under excitation.

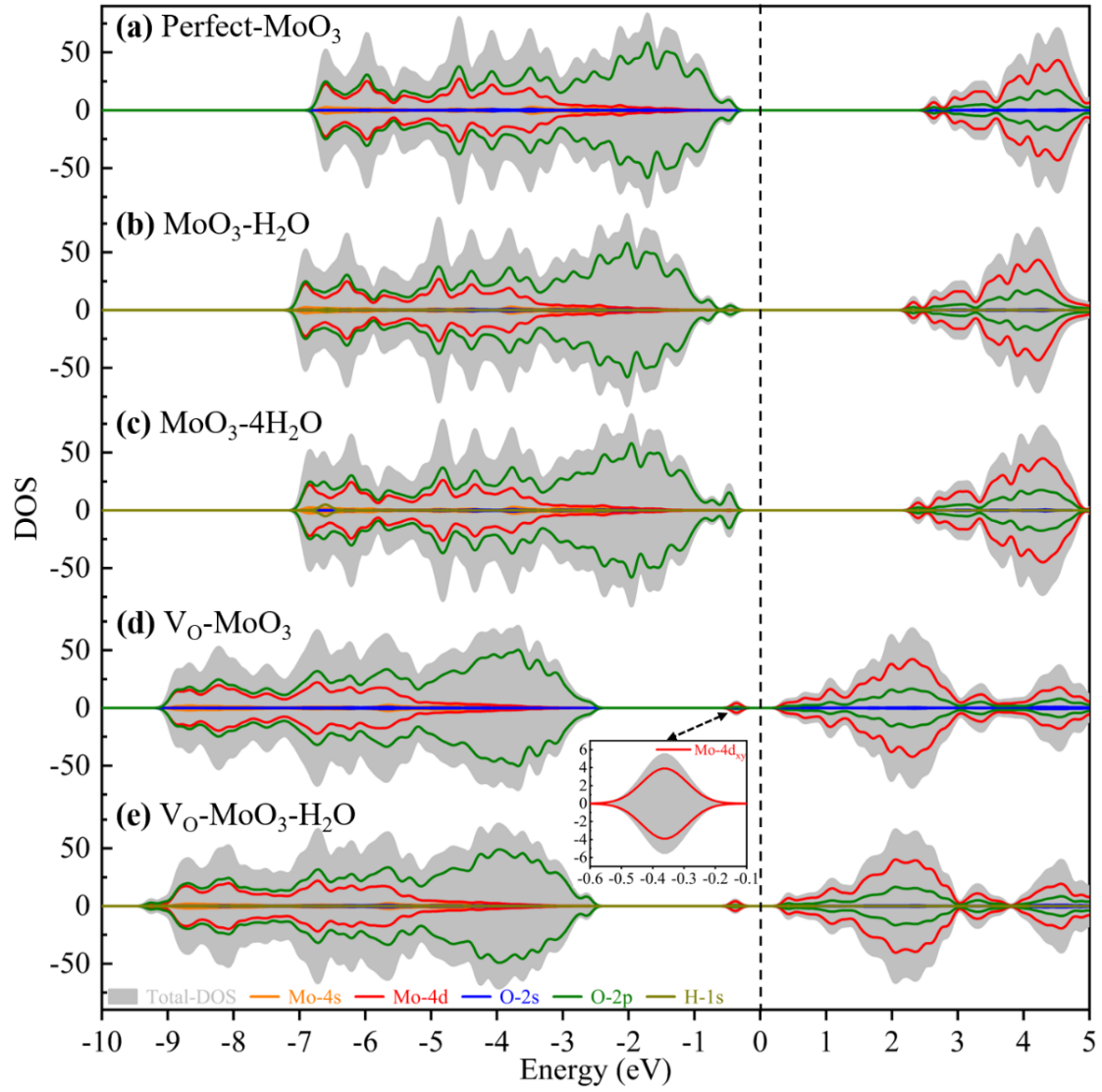


Fig. 6 PDOS of perfect-MoO₃ (a), MoO₃-H₂O (b), MoO₃-4H₂O (c), V_O-MoO₃ (d), and V_O-MoO₃-H₂O (e). Inset shows the enlargement of the defective state associated with V_O. The Fermi level is set as 0 and marked with a vertical dashed line.

Optical response of oxygen deficient surface and effect of moisture:

The optical absorption is crucial for the optoelectronic and photothermal application, while defect-free α -MoO₃ suffers from limited range of light absorption. Therefore, we conducted calculations on the optical absorption spectra of perfect-MoO₃, MoO₃-H₂O, V_O-MoO₃, and V_O-MoO₃-H₂O, and plotted the results in Fig. 7a and b. All MoO₃

systems exhibit anisotropic optical absorption. As shown in Fig. 7a, both the perfect MoO_3 and $\text{MoO}_3\cdot 4\text{H}_2\text{O}$ merely absorb ultraviolet (UV) light. However, there is a slight red-shift (inset of Fig. 7a) of absorption spectra with the increase of adsorbed H_2O molecules, which is due to the intermediate gap state extending to the edge of valence band (Fig. 6b and c). Meaningfully, there are strong NIR absorption from 0.5 to 1.3 eV and weak visible light absorption in $\text{V}_\text{O}\text{-MoO}_3$ and $\text{V}_\text{O}\text{-MoO}_3\text{-H}_2\text{O}$ (Fig. 7b), which are attributed to the excitations from intermediate state to CBM and VBM to intermediate state, respectively. Our calculation results may explain the previous experimental results where promoted light adsorption and LSPR effect by introduction of V_O for photo-thermal synergistic catalytic and photothermal therapy⁵³⁻⁵⁵. As shown in the schematic diagrams in Fig. 7c and d, the perfect- MoO_3 and $\text{MoO}_3\text{-H}_2\text{O}$ only absorb UV light through excitations from the VBM to CBM. In contrast, $\alpha\text{-MoO}_3$ with V_O can not only absorb UV light but also absorb NIR light through the intermediate state with excitation from Mo-4d_{xy} to O-2p empty levels. Hence, the optical properties of $\alpha\text{-MoO}_3$ can be modulated by proper introduction of V_O to achieve applications in photocatalysis, photothermal therapy, and photodetector.

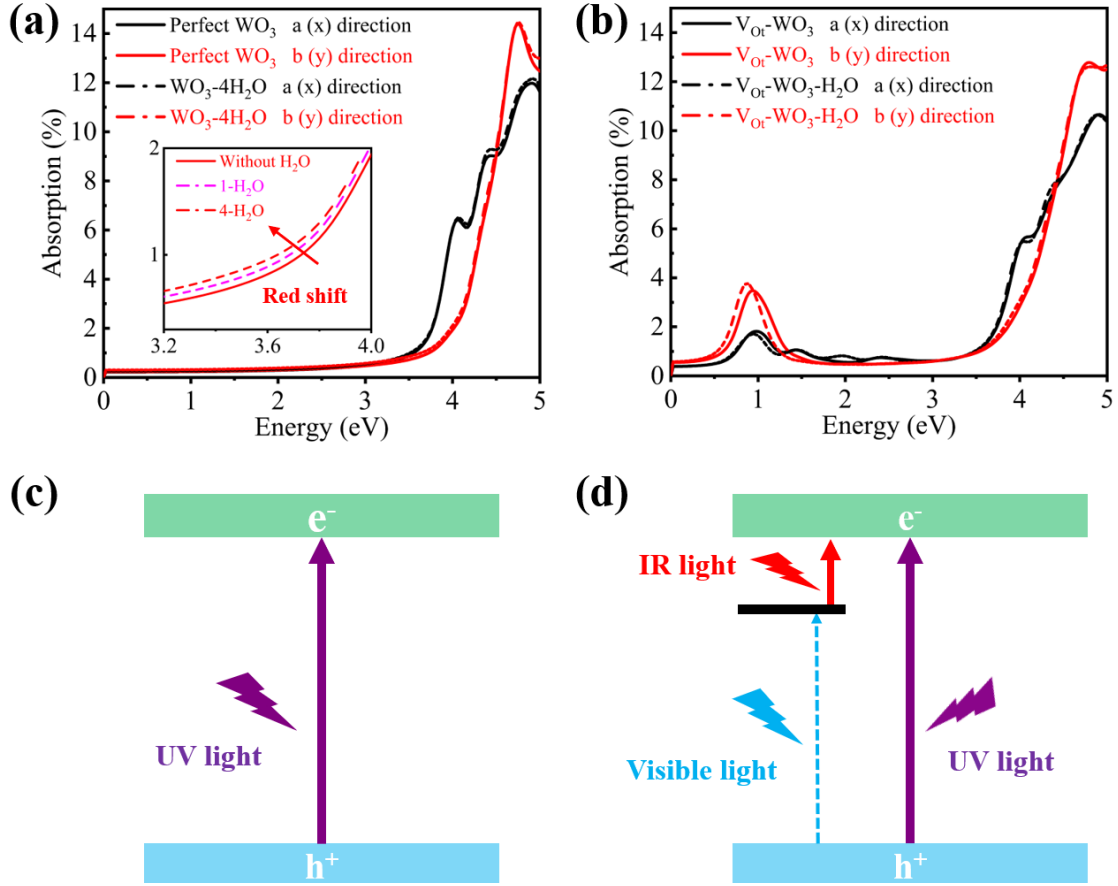


Fig. 7 The absorption spectra of perfect-MoO₃ and MoO₃-4H₂O (a), V_O-MoO₃ and V_O-MoO₃-H₂O (b). Schematic energy band diagram of optical absorption in MoO₃-H₂O (c) and V_O-MoO₃-H₂O (d). The inset in (a) show a red-shift of absorption spectra with the increase of H₂O molecules.

Variation of work function with oxygen deficiency and H₂O adsorption:

Fig. 8 summarizes the alignment of the VBM and CBM with respect to the vacuum level for different systems based on the HSE06 calculation. The difference between CBM and VBM of different systems is slight, but the position of the Fermi level is quite different. The positions of the Fermi level are -6.96, -5.64, -3.93 and -3.85 eV for perfect-MoO₃, MoO₃-H₂O, V_O-MoO₃, and V_O-MoO₃-H₂O, respectively. The work

functions were also calculated accordingly based on $\varphi = E_{\text{vac}} - E_{\text{F}}$, where φ , E_{vac} , and E_{F} represent the work function, vacuum level, and Fermi level, respectively. The calculated φ are 9.07, 8.74, 7.03, and 6.96 eV for perfect-MoO₃, MoO₃-H₂O, V_O-MoO₃, and V_O-MoO₃-H₂O, respectively. The calculated work function of V_O-MoO₃, and V_O-MoO₃-H₂O are in good agreement with the experimental result obtained by UPS, where the work function and Fermi level of near-stoichiometric bulk MoO_{3-x} are 6.89 eV and 0.39-0.59 eV below the CBM, respectively⁴⁸. Furthermore, the introduction of intermediate state can effectively enhance the conductivity of V_O-MoO₃ or MoO_{3-x} which reduces the Fermi energy to slightly above the VBM of the active materials in solar cells, and make oxygen deficient MoO_{3-x} promising as a hole transport layer in solar cells and LEDs^{56, 57}. Accordingly, introduction of V_O dramatically modulates the work function, which in turn can affect the height of the Schottky barrier or formation of Ohmic contact in practical applications. In ultrathin monolayer or few-layer MoO₃, the weak electronic screening may imply an appreciable width of the depletion/accumulation regions. In contrast, the adsorption of H₂O makes a weak effect on the work function, which also forms an intermediate state and marginally shifts the position of the CBM and VBM.

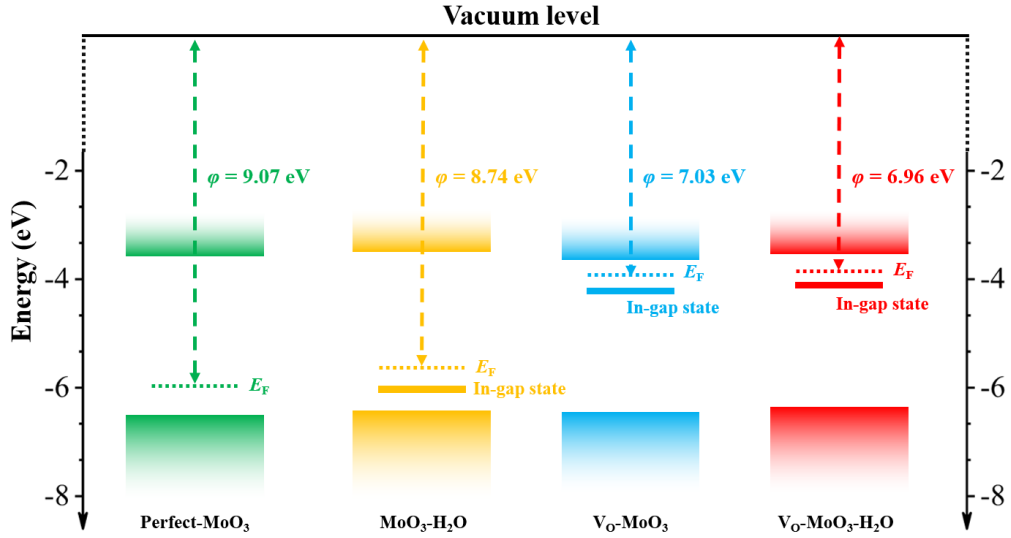


Fig. 8 Work functions of perfect-MoO₃, MoO₃-H₂O, V_O-MoO₃, and V_O-MoO₃-H₂O calculated by HSE06 method. The Fermi level is marked with a horizontal dashed line.

4. Conclusion

In conclusion, we have examined the adsorption behavior of H₂O molecules on the surface and oxygen vacancies of monolayer α -MoO₃, as well as the electronic properties, interfacial charge transfer, work function, and optical properties. Our results indicates that the adsorption of H₂O molecules on the surface of α -MoO₃ will introduce an intermediate state close to the edge of valence band and allowing the thermally activated conduction, which is necessary for monitoring relative humidity in moisture-sensitive environment. For oxygen deficient α -MoO₃, oxygen vacancies at the terminal and asymmetric sites are more energetically favored and those vacancies create defective localized levels slightly beneath the CBM. The depletion of oxygen atoms makes the dangling Mo atoms reduced and promotes the adsorption of H₂O. Interestingly, the H₂O induced shallow level slightly above VBM of perfect MoO₃ is quenched when H₂O is anchored at the V_O site. While the H₂O donates electrons to

MoO₃ for adsorbing above perfect lattice, it receives electrons when adsorbing above V_O site. This strong interaction between V_O-H₂O complex suggests that oxygen deficient MoO₃ could be a promising moisture sensor which can modulate the performance of conductivity and optoelectronics. Our work reveals that the presence of V_O and H₂O could alter the work function, the carrier density and optical response which are conducive to the application in optoelectronics, sensing, and photothermal therapy.

Conflicts of interest

The authors declare that they have no known competing financial interests or personal relationships that could have appeared to influence the work reported in this paper.

Acknowledgments

The authors acknowledge the funding support from the 100 Talents Program of Sun Yat-sen University (Grant 76220-18841201), the University of Macau (SRG2019-00179-IAPME) and the Science and Technology Development Fund from Macau SAR (FDCT-0163/2019/A3), the Natural Science Foundation of China (Grant 22022309) and Natural Science Foundation of Guangdong Province, China (2021A1515010024).

Reference

1. P. Kumbhakar, C. Chowde Gowda, P. L. Mahapatra, M. Mukherjee, K. D. Malviya, M. Chaker, A. Chandra, B. Lahiri, P. M. Ajayan, D. Jariwala, A. Singh and C. S.

- Tiwary, *Mater. Today*, 2021, **45**, 142-168.
2. J. M. Jeong, S. H. Park, H. J. Park, S. B. Jin, S. G. Son, J. M. Moon, H. Suh and B. G. Choi, *Adv. Funct. Mater.*, 2021, **31**.
 3. Y. Xiong, W. Liu, X. Qiao, X. Song, S. Wang, X. Zhang, X. Wang and J. Tian, *Sens. Actuator B Chem.*, 2021, **346**.
 4. X. Jin, S. Y. Son, M. G. Kim and S.-J. Hwang, *Nano Energy*, 2020, **78**.
 5. S. Liu, L. Wang, X. Feng, Z. Wang, Q. Xu, S. Bai, Y. Qin and Z. L. Wang, *Adv. Mater.*, 2017, **29**.
 6. Y. Zhao, C. Chang, F. Teng, Y. Zhao, G. Chen, R. Shi, G. I. N. Waterhouse, W. Huang and T. Zhang, *Adv. Energy Mater.*, 2017, **7**.
 7. Z. Su, W. Ren, H. Guo, X. Peng, X. Chen and C. Zhao, *Adv. Funct. Mater.*, 2020, **30**.
 8. S. R. Sahu, V. R. Rikha, P. Haridoss, A. Chatterjee, R. Gopalan and R. Prakash, *Adv. Energy Mater.*, 2020, **10**.
 9. X. He, H. Zhang, X. Zhao, P. Zhang, M. Chen, Z. Zheng, Z. Han, T. Zhu, Y. Tong and X. Lu, *Adv. Sci.*, 2019, **6**, 1900151.
 10. W. Ma, P. Alonso-Gonzalez, S. Li, A. Y. Nikitin, J. Yuan, J. Martin-Sanchez, J. Taboada-Gutierrez, I. Amenabar, P. Li, S. Velez, C. Tollan, Z. Dai, Y. Zhang, S. Sriram, K. Kalantar-Zadeh, S. T. Lee, R. Hillenbrand and Q. Bao, *Nature*, 2018, **562**, 557-562.
 11. G. Hu, Q. Ou, G. Si, Y. Wu, J. Wu, Z. Dai, A. Krasnok, Y. Mazor, Q. Zhang, Q. Bao, C. W. Qiu and A. Alu, *Nature*, 2020, **582**, 209-213.

12. Q. Zhang, Q. Ou, G. Hu, J. Liu, Z. Dai, M. S. Fuhrer, Q. Bao and C. W. Qiu, *Nano Lett.*, 2021, **21**, 3112-3119.
13. G. Alvarez-Perez, T. G. Folland, I. Errea, J. Taboada-Gutierrez, J. Duan, J. Martin-Sanchez, A. I. F. Tresguerres-Mata, J. R. Matson, A. Bylinkin, M. He, W. Ma, Q. Bao, J. I. Martin, J. D. Caldwell, A. Y. Nikitin and P. Alonso-Gonzalez, *Adv. Mater.*, 2020, **32**, e1908176.
14. H. S. Kim, J. B. Cook, H. Lin, J. S. Ko, S. H. Tolbert, V. Ozolins and B. Dunn, *Nat. Mater.* , 2017, **16**, 454-+.
15. Y. Y. Zhang, P. Chen, Q. Y. Wang, Q. Wang, K. Zhu, K. Ye, G. L. Wang, D. X. Cao, J. Yan and Q. Zhang, *Adv. Energy Mater.*, 2021, **11**.
16. J. Yang, X. Xiao, P. Chen, K. Zhu, K. Cheng, K. Ye, G. L. Wang, D. X. Cao and J. Yan, *Nano Energy*, 2019, **58**, 455-465.
17. S. Feng, C. Liu, Q. Zhu, X. Su, W. Qian, Y. Sun, C. Wang, B. Li, M. Chen, L. Chen, W. Chen, L. Zhang, C. Zhen, F. Wang, W. Ren, L. Yin, X. Wang, H. M. Cheng and D. M. Sun, *Nat. Commun.*, 2021, **12**, 4094.
18. Z. Zhou, X. Wang, H. Zhang, H. Huang, L. Sun, L. Ma, Y. Du, C. Pei, Q. Zhang, H. Li, L. Ma, L. Gu, Z. Liu, L. Cheng and C. Tan, *Small*, 2021, **17**, e2007486.
19. M. Zhou, Y. Liu, Y. Su and Q. Su, *Adv. Healthcare Mater.*, 2021, DOI: 10.1002/adhm.202101331, e2101331.
20. D. Kwak, M. J. Wang, K. J. Koski, L. Zhang, H. Sokol, R. Maric and Y. Lei, *ACS Appl. Mater. Interfaces*, 2019, **11**, 10697-10706.
21. K. Xu, N. B. Liao, W. Xue and H. M. Zhou, *Appl. Surf. Sci.*, 2020, **509**.

22. K. Xu, N. Liao, B. Zheng and H. Zhou, *Phys. Lett. A*, 2020, **384**.
23. C. Tan, X. Cao, X. J. Wu, Q. He, J. Yang, X. Zhang, J. Chen, W. Zhao, S. Han, G. H. Nam, M. Sindoro and H. Zhang, *Chem. Rev.*, 2017, **117**, 6225-6331.
24. W. Xu, L. Gan, R. Wang, X. Wu and H. Xu, *ACS Appl. Mater. Interfaces*, 2020, **12**, 19110-19115.
25. A. Favron, E. Gaufres, F. Fossard, A. L. Phaneuf-L'Heureux, N. Y. Tang, P. L. Levesque, A. Loiseau, R. Leonelli, S. Francoeur and R. Martel, *Nat. Mater.*, 2015, **14**, 826-832.
26. X. Chen, C. Tan, Q. Yang, R. Meng, Q. Liang, M. Cai, S. Zhang and J. Jiang, *J. Phys. Chem. C*, 2016, **120**, 13987-13994.
27. G. Kresse and J. Furthmuller, *Phys. Rev. B*, 1996, **54**, 11169-11186.
28. G. Kresse and J. Furthmuller, *Comput. Mater. Sci.*, 1996, **6**, 15-50.
29. J. P. Perdew, K. Burke and M. Ernzerhof, *Phys. Rev. Lett.*, 1996, **77**, 3865-3868.
30. S. Grimme, S. Ehrlich and L. Goerigk, *J. Comput. Chem.*, 2011, **32**, 1456-1465.
31. S. Grimme, J. Antony, S. Ehrlich and H. Krieg, *J. Chem. Phys.*, 2010, **132**.
32. J. Heyd, G. E. Scuseria and M. Ernzerhof, *J. Chem. Phys.*, 2003, **118**, 8207-8215.
33. V. Wang, N. Xu, J.-C. Liu, G. Tang and W.-T. Geng, *Comput. Phys. Commu.*, 2021, **267**.
34. Y. Cai, Q. Ke, G. Zhang, B. I. Yakobson and Y. W. Zhang, *J. Am. Chem. Soc.*, 2016, **138**, 10199-10206.
35. A. F. Kohan, G. Ceder, D. Morgan and C. G. V. d. Walle, *Phys. Rev. B*, 2000, **61**, 9.

36. C. G. Van de Walle and J. Neugebauer, *J. Appl. Phys.*, 2004, **95**, 3851-3879.
37. Y. Cai, H. Zhou, G. Zhang and Y.-W. Zhang, *Chem. Mater.*, 2016, **28**, 8611-8621.
38. S. O. Akande, A. Chroneos, M. Vasilopoulou, S. Kennou and U. Schwingenschlögl, *J. Mater. Chem. C*, 2016, **4**, 9526-9531.
39. M. V. Ganduglia-Pirovano, A. Hofmann and J. Sauer, *Surf. Sci. Rep.*, 2007, **62**, 219-270.
40. C. Meng, G. Zhao, X. R. Shi, P. Chen, Y. Liu and Y. Lu, *Sci. Adv.*, 2021, **7**.
41. Y. Liu, Y. Peng, M. Naschitzki, S. Gewinner, W. Schollkopf, H. Kühlenbeck, R. Pentcheva and B. Roldan Cuenya, *Angew. Chem. Int. Ed.*, 2021, **60**, 16514-16520.
42. A. A. Kistanov, Y. Cai, K. Zhou, S. V. Dmitriev and Y.-W. Zhang, *2D Mater.*, 2016, **4**.
43. Y. Cai, Q. Ke, G. Zhang and Y.-W. Zhang, *J. Phys. Chem. C*, 2015, **119**, 3102-3110.
44. A. A. Kistanov, Y. Q. Cai, D. R. Kripalani, K. Zhou, S. V. Dmitriev and Y. W. Zhang, *J. Mater. Chem. C*, 2018, **6**, 4308-4317.
45. N. Hamamoto, T. Tatsumi, M. Takao, T. Toyao, Y. Hinuma, K.-i. Shimizu and T. Kamachi, *J. Phys. Chem. C*, 2021, **125**, 3827-3844.
46. R. Coquet and D. J. Willock, *Phys. Chem. Chem. Phys.*, 2005, **7**, 3819-3828.
47. H. Xu and X. Zhou, *J. Appl. Phys.*, 2013, **114**.
48. M. T. Greiner, L. Chai, M. G. Helander, W.-M. Tang and Z.-H. Lu, *Adv. Funct. Mater.*, 2012, **22**, 4557-4568.
49. Y. Hu, X. Liu, S. Xu, W. Wei, G. Zeng, H. Yuan, Q. Gao, J. Guo, M. Chao and E.

- Liang, *J. Phys. Chem. C*, 2021, **125**, 10817-10823.
50. S. Patnaik, G. Swain and K. M. Parida, *Nanoscale*, 2018, **10**, 5950-5964.
 51. L. Liang, X. Li, Y. Sun, Y. Tan, X. Jiao, H. Ju, Z. Qi, J. Zhu and Y. Xie, *Joule*, 2018, **2**, 1004-1016.
 52. N. B. Liao, H. M. Zhou, B. R. Zheng and W. Xue, *IEEE Electr. Device L.*, 2018, **39**, 1760-1763.
 53. J. Li, Y. Ye, L. Ye, F. Su, Z. Ma, J. Huang, H. Xie, D. E. Doronkin, A. Zimina, J.-D. Grunwaldt and Y. Zhou, *J. Mater. Chem. A*, 2019, **7**, 2821-2830.
 54. F. Ye, D. Chang, A. Ayub, K. Ibrahim, A. Shahin, R. Karimi, S. Wettig, J. Sanderson and K. P. Musselman, *Chem. Mater.*, 2021, **33**, 4510-4521.
 55. J. Miao, Y. Cai, Y. N. Shao, G. L. Yang, H. Y. Huang, Z. W. Shang, J. J. Cheng, Y. W. Li and X. Q. Xu, *Appl. Mater. Today*, 2021, **23**.
 56. X. Liao, S. N. Habisreutinger, S. Wiesner, G. Sadoughi, D. Abou-Ras, M. A. Gluba, R. G. Wilks, R. Felix, M. Rusu, R. J. Nicholas, H. J. Snaith and M. Bar, *ACS Appl. Mater. Interfaces*, 2021, **13**, 17085-17092.
 57. Q. Wu, F. Cao, H. Wang, J. Kou, Z. H. Zhang and X. Yang, *Adv. Sci.*, 2020, **7**, 2001760.